

# ADVANCED MATERIALS

## Supporting Information

for *Adv. Mater.*, DOI 10.1002/adma.202210557

Liquid-Superspreading-Boosted High-Performance Jet-Flow Boiling for Enhancement of Phase-Change Cooling

*Zhe Xu, Peng Zhang, Chuanghui Yu, Weining Miao, Qiankun Chang, Ming Qiu, Yulong Li, Ye Tian\* and Lei Jiang*

Supporting Information

**Liquid-Superspreading-Boosted High-Performance Jet-Flow Boiling for Enhancement of Phase-Change Cooling**

*Zhe Xu, Peng Zhang, Chuanghui Yu, Weining Miao, Qiankun Chang, Ming Qiu, Yulong Li, Ye Tian<sup>\*</sup>, and Lei Jiang*

**This File Includes:****Experimental Section**

*Under-Liquid Bubble Adhesion Force Test in Heating Condition*

*Boiling Heat Transfer Performance Measurement*

*Phase-Change Cooling Performance Measurement*

**Figure S1.** SEM images of a designed periodic array structure on Cu surface by using a nano-second pulse laser fabricating technology.

**Figure S2.** Comparison on the  $C_6H_5F_9O$  liquid spreading capacity of different micro-/nano textured Cu surfaces.

**Figure S3.** A characteristic jet-flow boiling phenomenon of  $C_6H_5F_9O$  on the designed MN-Cu surface with phase-change bubbles rapidly ejected in multiple strip beams.

**Figure S4.** Comparison on adhesion force of a 5  $\mu$ L air bubble on different Cu surfaces under  $C_6H_5F_9O$  liquid at room temperature (25 °C) by using a classical testing method.

**Figure S5.** Solid-liquid-vapor contact state of the flat Cu and MN-Cu surfaces under different solid temperature. (a) Flat Cu,  $T_{solid} = 25$  °C; (b) Flat Cu,  $T_{solid} = 50$  °C; (c) MN-Cu,  $T_{solid} = 25$  °C; (d) MN-Cu,  $T_{solid} = 50$  °C.

**Figure S6.** Changes of the contact state between an expanding air bubble and the 50 °C solid substrate over time, related to Movie S2 and Movie S3. (a) Flat Cu; (b) MN-Cu.

**Figure S7.** 3D Morphology and SEM images of the Cu surfaces with different pyramid height (PH) but similar pyramid space (PS).

**Figure S8.** Static contact angle (CA) and spreading time of the Cu surfaces with different pyramid height.

**Figure S9.** Sliding time of a 5  $\mu$ L air bubble along the slightly sloping ( $\sim 0.35^\circ$ ) flat Cu (PH  $\sim 0.8$   $\mu$ m) and MN-Cu (PH  $\sim 134.4$   $\mu$ m) surfaces under  $C_6H_5F_9O$  liquid.

**Figure S10.** Boiling heat transfer performance of water on flat Cu (PH  $\sim 0.8$   $\mu$ m) and MN-Cu (PH  $\sim 134.4$   $\mu$ m) surfaces. (a) Critical heat flux (CHF); (b) Heat-transfer coefficient (HTC).

**Figure S11.** Optical microscopy images of MN-Cu surfaces with different groove space (GS) via a nano-second pulse laser fabrication.

**Figure S12.** *In situ* infrared thermograph of different hot MN-Cu surfaces with controllable groove space (GS) at a structure region 5 mm  $\times$  15 mm.

**Figure S13.** *In situ* observation and mechanism analysis of an initial jet-flow boiling bubble on a MN-Cu surface.

**Figure S14.** Logarithmic plot of the spreading diameter of  $C_6H_5F_9O$  liquid versus spreading time on the MN-Cu surface.

**Figure S15.** 3D Morphology images of different MN-Cu surfaces with increasing pyramid space (PS) but relatively similar pyramid height (PH) tuned by a pulse-overlapped laser-fabricating route.

**Figure S16.** SEM image of MN-Cu surfaces with controllable pyramid space (PS) but similar pyramid height (average PH  $\sim 134.4 \mu\text{m}$ ).

**Figure S17.** Comparison on departure diameter of an initial phase-change vapor bubble away from different MN-Cu surfaces with controllable pyramid space (PS) under  $\text{C}_6\text{H}_5\text{F}_9\text{O}$  liquid.

**Figure S18.** Phase-change cooling performance experimental setup.

**Figure S19.** Real demo of a commercial jet-flow-based boiling enhancement plate (JFBEP) for high-performance CPU phase-change cooling.

**Figure S20.** Boiling heat transfer performance experimental setup.

**Table S1.** Comparison on enhanced boiling heat transfer performance of the previously reported micro-/nanostructured Cu surfaces.

**Table S2.** Basic properties of three different commercial fluorinert electronic liquids (FELs) from 3M company, USA.

Capture: **Movie S1.** Super-spreading of a  $2 \mu\text{L}$   $\text{C}_6\text{H}_5\text{F}_9\text{O}$  liquid droplet on MN-Cu surface.

Capture: **Movie S2.** Dynamic under-liquid bubble adhesion process of an expanding bubble ( $\sim 2.1 \mu\text{L} \sim 3.6 \mu\text{L}$ ) on flat Cu surface at  $50 \text{ }^\circ\text{C}$  in  $\text{C}_6\text{H}_5\text{F}_9\text{O}$  liquid.

Capture: **Movie S3.** Dynamic under-liquid bubble adhesion process of an expanding bubble ( $\sim 2.1 \mu\text{L} \sim 3.6 \mu\text{L}$ ) on MN-Cu surface at  $50 \text{ }^\circ\text{C}$  in  $\text{C}_6\text{H}_5\text{F}_9\text{O}$  liquid.

Capture: **Movie S4.** *In situ* boiling comparison of a Cu plate with asymmetric structures in  $\text{C}_6\text{H}_5\text{F}_9\text{O}$  liquid at a low superheat  $\sim 3.0 \text{ }^\circ\text{C}$ .

Capture: **Movie S5.** Rolling and coalescence of the onset of jet-flow boiling (OJB) bubbles on a flat Cu surface.

Capture: **Movie S6.** A single strip of jet-flow boiling bubbles ejected from the bottom of micro-groove on a designed MN-Cu surface.

Capture: **Movie S7.** *In situ* observation of nucleation, growth, and departure behaviors of an initial jet-flow boiling bubble on a designed MN-Cu surface with narrow pyramid space.

Capture: **Movie S8.** *In situ* observation of nucleation, growth, and departure behaviors of an initial jet-flow boiling bubble on a designed MN-Cu surface with wide pyramid space.

## Experimental Section

*Under-Liquid Bubble Adhesion Force Test in Heating Condition:* To investigate the adhesion force in heating environment (at a constant solid temperature of 50 °C), a measuring method was conducted by catching the optical profile of an expanding bubble with continuous liquid-vapor phase change, and then calculating corresponding forces during a contacting, adhering, and squeezing processes with a fixed distance between injecting needle and solid substrate. In our experiments, the volume of the expanding bubbles for comparison on flat Cu and MN-Cu changes from ~2.1  $\mu\text{L}$  to ~3.6  $\mu\text{L}$  within ~7.5 s. Final under-liquid bubble adhesion forces were obtained on a professional algorithm implemented as a DAF (drop adhesion force) module in the software “SurfaceMeter” delivered with a Surface Analyser (LSA100, Lauda Scientific, Germany).

The knowledge of the droplet shape allows a direct calculation of attractive force.<sup>[1]</sup> The interactive force ( $F$ ) between a droplet and a solid surface consists of surface tension ( $F_s$ ) and capillary pressure ( $F_p$ ) components. The surface tension force is the axial component of liquid-fluid interfacial tension acting along the perimeter of triple contact line. The capillary pressure force (acting over the contact area) is caused by the curvature of liquid bridge.

Combination of these two forces is presented in the following equation (1):<sup>[1,2]</sup>

$$F = F_s - F_p = 2\pi R \gamma \sin\theta - \pi R^2 \Delta P \quad (1)$$

where  $R$  is the radius of bubble base that is in contact with substrate,  $\gamma$  is the liquid-fluid interfacial tension,  $\theta$  is the contact angle and  $\Delta P$  is the Laplace pressure difference. The Laplace pressure difference can be either positive or negative, depending on the shape of the droplet.

At a hydrostatic equilibrium, the profile of a drop or meniscus can be described by the following Laplace-Young equation (2):

$$C_0 - \beta \left( \frac{z}{b} \right) = \frac{1}{r_1/b} + \frac{1}{r_2/b} \quad (2)$$

$$\beta = \Delta\rho g b^2 / \gamma \quad (3)$$

where  $b$  is a reference dimension (e.g., the contact radius at  $z=0$  or at  $z=h$ , where  $h$  is the height of drop),  $r_1$  and  $r_2$  the main radii of curvature at  $z=z$ , the system bond parameter as given by equation (3),  $\Delta\rho$  the density difference between the liquid/fluid-phase, and  $C_0$  a system constant. Under the assumption of rotational symmetry (axis-symmetry), this equation can be evaluated numerically in a similar way.<sup>[3]</sup> By fitting the profile of a drop/meniscus to this equation, all unknown parameter values, including surface/interfacial tension  $\gamma$ , contact angle  $\theta$ , contact diameter CD (and hence the perimeter of triple contact line) or area A (drop

volume/surface area), Laplace-Young capillary pressure difference  $\Delta P$  at the contact level ( $z = 0$ ), can be exactly determined.

The adhesion force  $F$  can then be computed as the balance force between the interfacial tension force  $F_s$  and the force due to the capillary pressure difference  $F_p$ . During evaluation, no assumptions, such as zero gravity, fixed contact angle or fixed contact radius, had been made.

*Boiling Heat Transfer Performance Measurement:* The basic pool boiling device consisted of a glass chamber (length, width, and height: 120 mm, 120 mm, and 120 mm, respectively) with a glass fixture on the top and a polyetheretherketones (PEEK) fixture at the bottom (Figure S20 a). A copper sheet was inserted into the PEEK fixture and locked via a stainless-steel fixture tightly, where a 3 mm-thick polytetrafluoroethylene (PTFE) plate and a 2 mm-thick PEEK plate were sandwiched and used as the thermal insulator, respectively. At the top of glass fixture, a reflux condenser was installed for allowing the condensed water to return back to the chamber and a thermocouple was inserted into the chamber for assisting the PID controller of the liquid temperature. At the bottom of PEEK fixture, an immersion heater (NCHW-1, 220 V, 100 W) was used to maintain the saturation temperature (100 °C for water) in the chamber by preventing heat loss. Before experimental measurements, the immersion heater was used to pre-heat 1000 ml of de-ionized water to degas the liquid by boiling for 60 minutes to remove the dissolved air. We chose the upper surface of copper sheet as the boiling surface for testing (Figure S20 a<sub>i</sub>) with its circle diameter of 20.0 mm (area  $\approx 314.16 \text{ mm}^2$ ), on which the flat Cu and MN-Cu surfaces were directly fabricated by either mechanical polish or laser-fabrication. To achieve super-spreading of water, both samples are undergone an air plasma treatment (200 W, 10 min) before the boiling test. Four internal T-type thermocouples with a constant neighboring distance ( $d = 5.0 \text{ mm}$ ) were inserted into the axial center of copper sheet to record the site temperatures ( $T_1, T_2, T_3$ , and  $T_4$ ), which could be real-time monitored by a paperless thermal recorder (NHR-6800, Fujian Shunchang Precise-Instrument Co., Ltd. China). As the variation of temperature was less than 0.1 °C per 5 min, the temperature gradient ( $\nabla T$ ) of the copper sheet interior would reach steady state. In this case, at least 60 data points were collected and used for calculating the average values of ( $T_1, T_2, T_3$ , and  $T_4$ ), corresponding to each heating power. Accordingly, the heat flux ( $q$ ) can be obtained by the following equations (4-6):

$$q = k\nabla T = -k \frac{\sum_{i=1}^4 (d_i - \bar{d})(T_i - \bar{T})}{\sum_{i=1}^4 (d_i - \bar{d})^2} \quad (4)$$

$$\bar{T} = \frac{1}{4} (T_1 + T_2 + T_3 + T_4) \quad (5)$$

$$\bar{d} = \frac{1}{4}(d_1 + d_2 + d_3 + d_4) \quad (6)$$

where  $d_1$ ,  $d_2$ ,  $d_3$ , and  $d_4$  is the distance from the first, second and third thermocouple to the boiling surface, respectively;  $\bar{d}$  is the average value of  $d_1$ ,  $d_2$ ,  $d_3$ , and  $d_4$ ;  $\bar{T}$  is the average value of  $T_1$ ,  $T_2$ ,  $T_3$ , and  $T_4$ ;  $k$  is the thermal conductivity of copper. Likewise, the degree of wall superheat ( $\Delta T$ ) can be calculated by equation (7):

$$\Delta T = T_s - T_w = \left( \bar{T} - \frac{q}{k} \bar{d} \right) - T_w \quad (7)$$

As a result, boiling heat transfer coefficient (HTC) can be obtained by the equation (8):

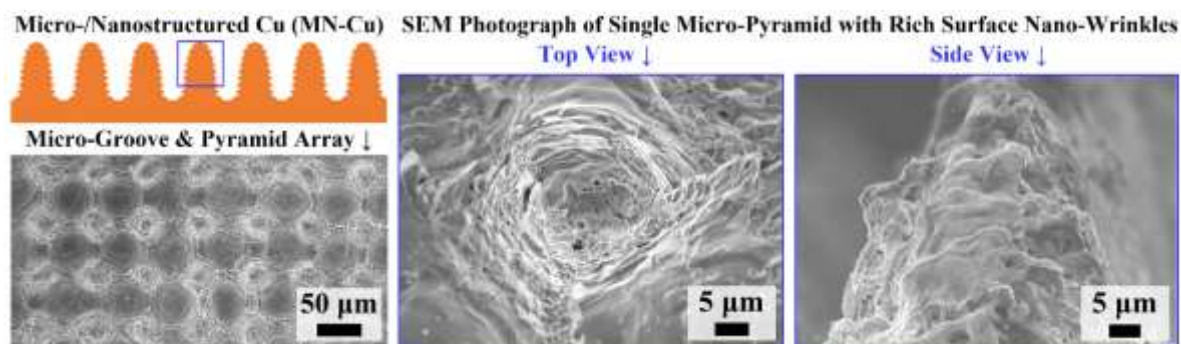
$$\text{HTC} = kVT/\Delta T \quad (8)$$

At the bottom of copper sheet (Figure S20 a<sub>ii</sub>), five silicon nitride heating rods (60 V, 200 W) were threaded and controlled with a DC power supply (DP3020, Shenzhen Mestek Instrument Co., Ltd. China, maximum input power of 1000 W). For each test, a tunable increase of the input power had been applied for enhancing the superheat until a drop of heat flux (or even a film boiling) was observed. To satisfy one-dimensional axial steady-state heat conduction, a 10.0 mm-thick PTFE shell was equipped outside the copper sheet as a thermal insulator.

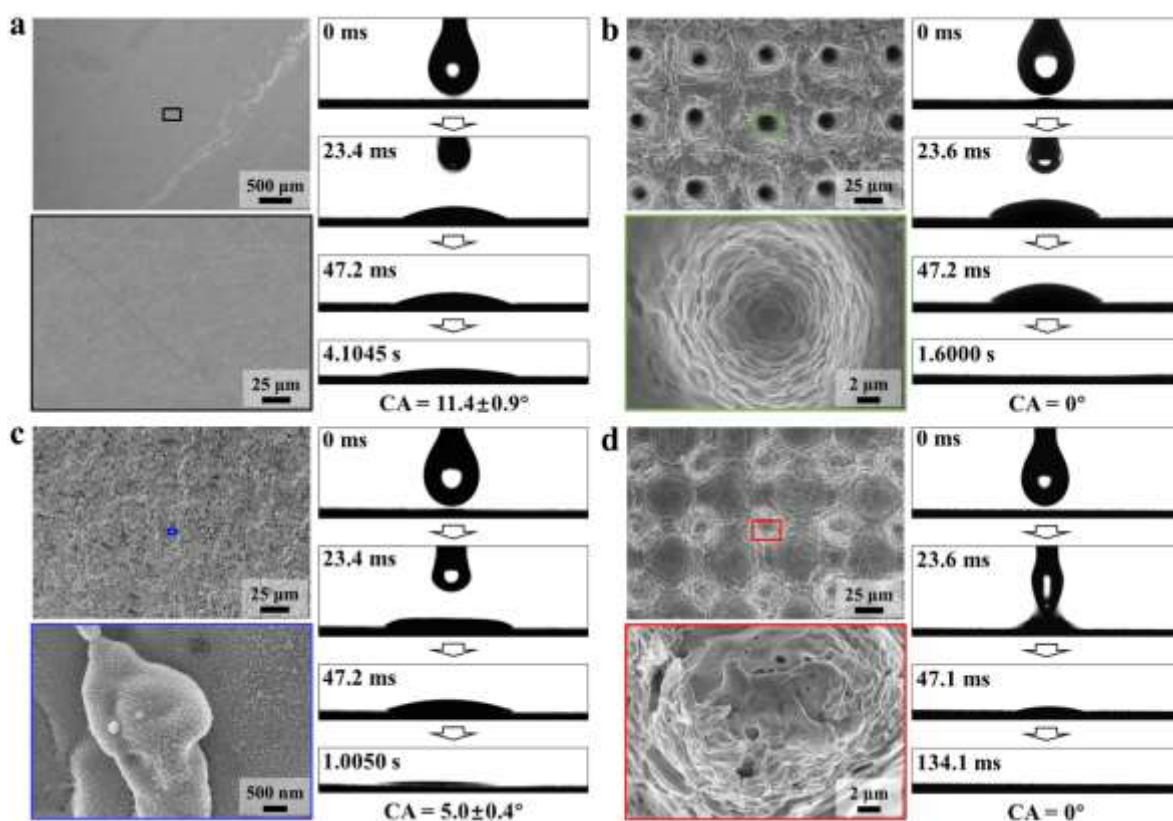
To save the dosage of boiling liquid as well as prevent the rapid escape of evaporated liquid, a modified pool boiling device (Figure S20 b and c) for  $\text{C}_6\text{H}_5\text{F}_9\text{O}$  liquid (purchased from Shanghai Aladdin Biochemical Technology Co., Ltd. China) was established by adding an inner glass sleeve (circle diameter: 56 mm) and applying a water seal with a reflux condenser. Compared with the basic pool boiling device for water (1000 ml), the volume of  $\text{C}_6\text{H}_5\text{F}_9\text{O}$  in inner glass sleeve was confined up to only 120 ml at the same liquid level. The water seal was formed by pouring 120 ml de-ionized water into the glass sleeve, which was kept stable just due to the natural immiscible property and density difference of water and  $\text{C}_6\text{H}_5\text{F}_9\text{O}$  (relative density 1.42) without extra partition. The reflux condenser with a pumped  $-20\text{ }^\circ\text{C}$  coolant (purchased from Turtle Wax Inc., America, G-4083R, anti-freezing, working temperature  $-42\sim 0\text{ }^\circ\text{C}$ ) in a U-tube was conducted to prevent the loss of  $\text{C}_6\text{H}_5\text{F}_9\text{O}$  liquid and provide an in-time back-flow during the long-term boiling measurement. The coolant temperature ( $-20\text{ }^\circ\text{C}$ ) was well kept using a 2 L low temperature cooling bath (DHJF-4002, Zhengzhou Greatwall Scientific Industrial and Trade Co., Ltd. China). Besides, the other chamber outside the glass sleeve could be filled with water (600 ml) and used as a hot bath by maintaining the saturation temperature at  $76\text{ }^\circ\text{C}$  for  $\text{C}_6\text{H}_5\text{F}_9\text{O}$ . Before each experimental measurement, the immersion heater was used to pre-heat the liquid by boiling for 60 minutes. Other operations as well as the data collections (such as OJB, CHF, HTC curves) were similar as those in our basic pool boiling device.

*Phase-Change Cooling Performance Measurement:* Our phase-change cooling experimental setup (Figure S18 a) consisted of a heating device, a boiling chamber, and a condensation system. In the heating device, an electric heater metal square (length, width, and height: 40 mm, 40 mm, and 15 mm) was used as heat source with temperature control range from room temperature to 350 °C (accuracy  $< \pm 1.0$  °C), which could provide a theoretical heat flux at 220 W/cm<sup>2</sup>. Before the measurements, a standard copper sheet (thickness: 4 mm) was connected with the metal heater, bonded by using a thermal silicone grease, and mechanically fastened with a PTFE fixture. Three internal T-type thermocouples were inserted at into the copper sheet (Figure S18 b) along three symmetrically distributed channels, which was drilled at a distance of 1 mm under its upper surface. An average value of the different thermocouple temperatures ( $T_1, T_2, T_3$ ) was calculated as the Cu temperature for evaluating phase-change cooling performance. Long-term stability tests of phase-change cooling were achieved by capturing real-time temperatures of the copper sheets for every 0.5 s from a paperless thermal recorder (NHR-6800, Fujian Shunchang Precise-Instrument Co., Ltd. China). Different MN-Cu surfaces were constructed on the upper side of copper sheet (structured region) with a constant circle area (diameter: 36 mm) via laser-fabrication. The condensation system was similar with the modified pool boiling device for C<sub>6</sub>H<sub>5</sub>F<sub>9</sub>O to prevent the loss of FELs and maintain the liquid level, which consisted of a water seal with the reflux condenser containing a pumped -20 °C coolant in a U-tube. It ensured that the escaping FEL vapor could be in time condensed and finally flow back through the water seal. Three different commercial FELs (3M\_Novec\_7100/7200/7300, purchased from 3M Company Co., Ltd. USA) were used for testing the phase-change cooling performance, keeping a volume rate of 1:1 with the sealing water. Another external thermocouple was insert into the boiling chamber, keeping at a distance of 1 mm from the upper side of copper sheet, and the FEL temperature was recorded by every 0.5 min (3M\_Novec\_7100/7200) or 1 min (3M\_Novec\_7300) during gradually heating. Additionally, for the sake of observing the phase-change bubbles from a horizontal view, another special copper sheet by adding an extra cylinder platform (height: 16 mm, diameter: 36 mm) onto the as-mentioned standard copper sheet was prepared (Figure S18 c). Four internal T-type thermocouples with a constant neighboring distance ( $d = 5.0$  mm) were inserted into the axial center of cylinder platform to record the site temperatures ( $T_1, T_2, T_3$ , and  $T_4$ ), which was used to obtain the data of the real-time superheat and heat flux. The PUE data of a phase-change cooling system equipped with JFBEP products exclusively on over 100 pieces of CPU chips in real-life supercomputers were obtained by an authorized organization (National Supercomputing Center in Xi'an, China). According to the National

Standards (GB/T 8222-2008, GB 40879-2021) in China, the actual measurements required 30 mins for each with three different loads (20%, 60%, and 100%, respectively) and an average value was obtained from the recording data of total power consumption and information technology (IT) equipment power consumption by every 5 mins. To deal with the heat management of similar microprocessors by single-phase liquid cooling (based on cold plate technology), the PUE data was obtained from another authorized organization (Beijing Energy Conservation and Environmental Protection Center, China).

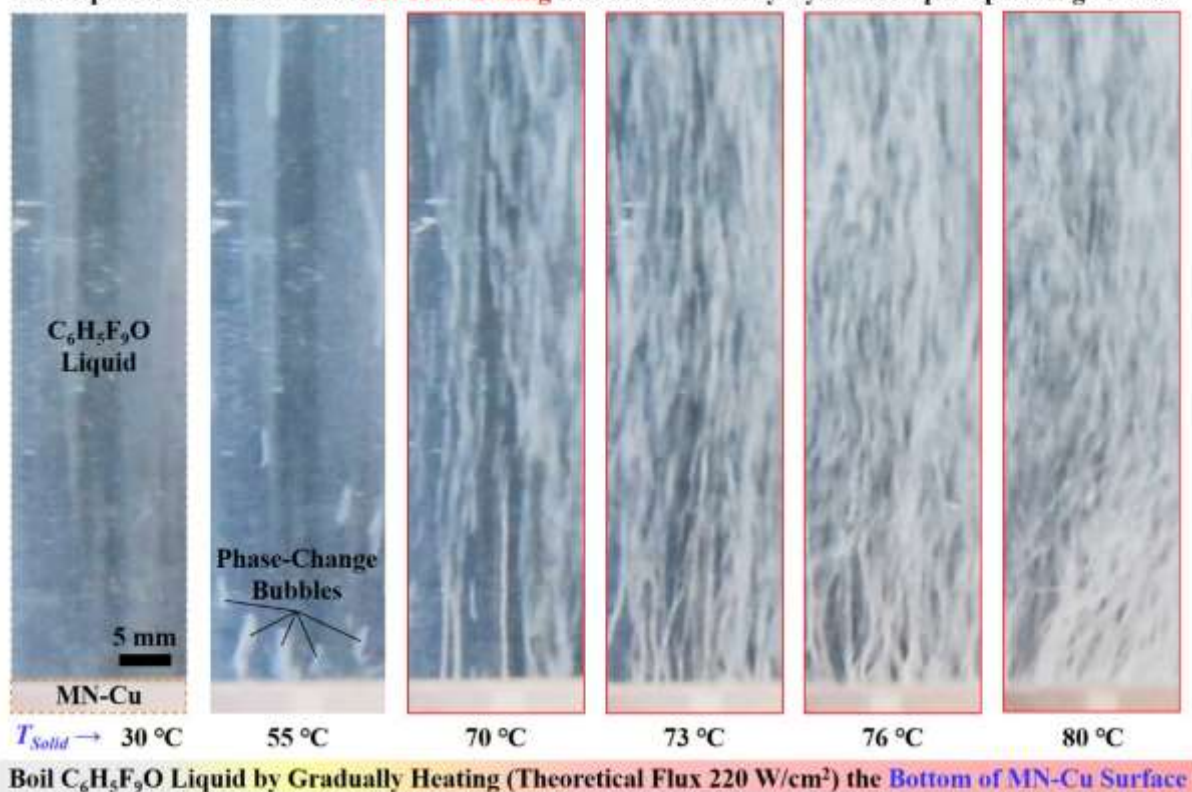


**Figure S1.** SEM images of a designed periodic array structure on Cu surface by using a nano-second pulse laser fabricating technology, consisting of a regular micro-groove/pyramid array with rich secondary nano-wrinkles on its surface.



**Figure S2.** Comparison on the  $C_6H_5F_9O$  liquid spreading capacity of different micro-/nano textured Cu surfaces, volume of the spreading liquid droplet  $2 \mu\text{L}$ . (a) Flat Cu; (b) Micro-pore dominant with minority of nano-wrinkles; (c) Nano-wrinkle dominant with rich nano-particles; (d) Micro-/nano-coordinated structures (MN-Cu).

As shown, a  $2 \mu\text{L}$   $C_6H_5F_9O$  liquid droplet needs 4.1045 s to spread on the flat Cu surface, maintaining an apparent contact angle of  $11.4 \pm 0.9^\circ$ . The nano-wrinkle dominant structures can accelerate this liquid spreading process and reach a much lower contact angle of  $5.0 \pm 0.4^\circ$  within 1.0050 s. The micro-pore dominant structures obtain a nearly  $0^\circ$  contact angle (called “super-spreading”), but it takes longer time (1.6000 s). The micro-/nano-coordinated structures strongly reduce the super-spreading time to  $\sim 134.1$  ms, which is faster than that in most reported literatures.<sup>[4]</sup>

Development of Characteristic **Jet-Flow Boiling** Bubbles Boosted by Dynamic Super-Spreading Process

**Figure S3.** A characteristic jet-flow boiling phenomenon of  $C_6H_5F_9O$  on the designed MN-Cu surface with phase-change bubbles rapidly ejected in multiple strip beams.

During jet-flow boiling, the number of visible, independent strip beams increases with the rising of solid temperature (55, 70, 73, 76, and 80 °C). Furthermore, there is little distinct mutual coalescence of jet-flow strips even at high solid temperature (80 °C), illustrating that the MN-Cu surface prevents the disperse phase-change bubbles merging into a vapor film.

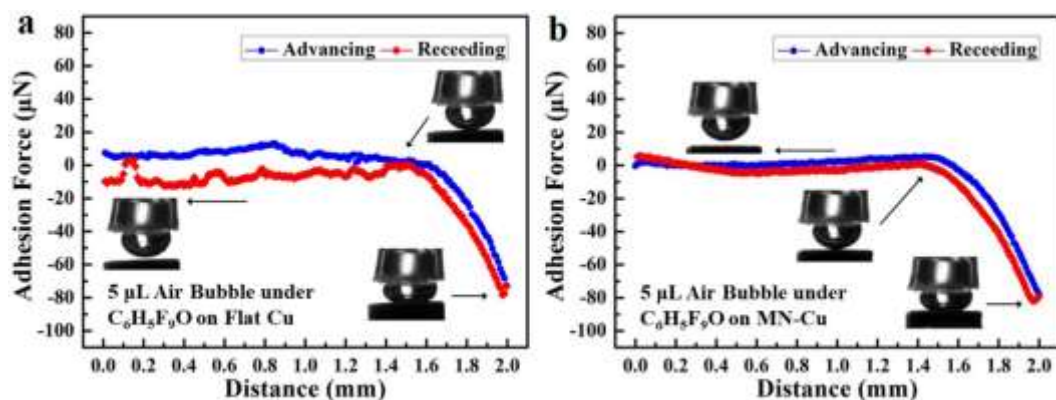


**Figure S4.** Comparison on adhesion force of a 5 µL air bubble on different Cu surfaces under C<sub>6</sub>H<sub>5</sub>F<sub>9</sub>O liquid at room temperature (25 °C) by using a classical testing method. (a) Flat Cu surface; (b) MN-Cu surface.

Both of them exhibit an ultra-low under-liquid bubble adhesion force ( $\sim 0$  µN) due to lack of liquid-vapor phase-change. It tends to form a stable pre-wetting liquid layer, by which a direct solid-vapor contact is limited.

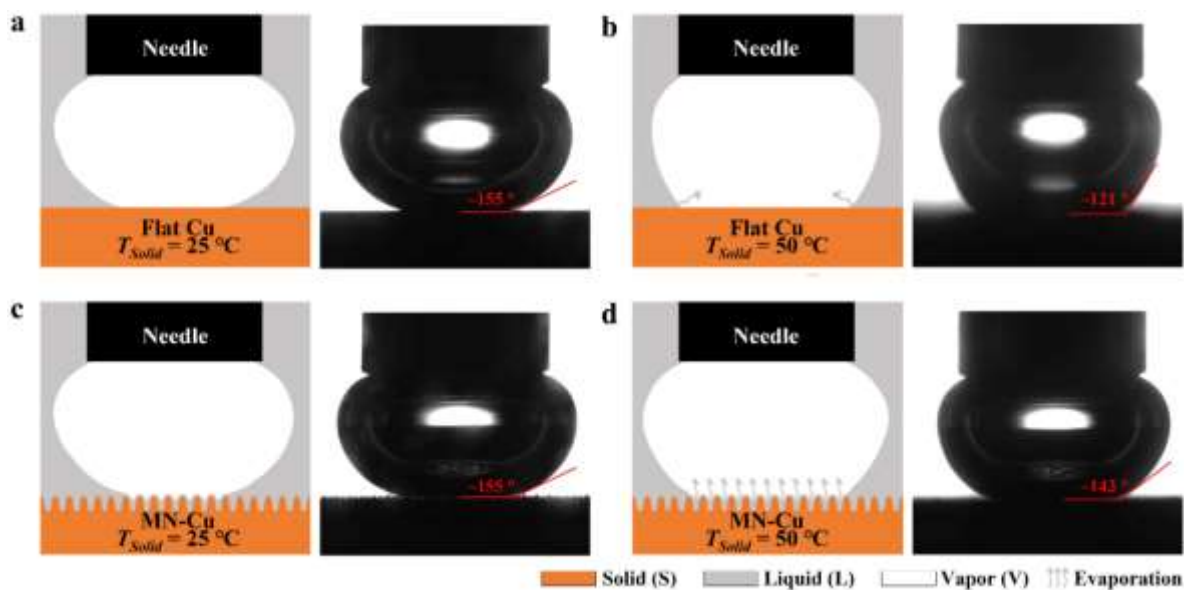


**Figure S5.** Solid-liquid-vapor contact state of the flat Cu and MN-Cu surfaces under different solid temperature. (a) Flat Cu,  $T_{solid} = 25\text{ }^{\circ}\text{C}$ ; (b) Flat Cu,  $T_{solid} = 50\text{ }^{\circ}\text{C}$ ; (c) MN-Cu,  $T_{solid} = 25\text{ }^{\circ}\text{C}$ ; (d) MN-Cu,  $T_{solid} = 50\text{ }^{\circ}\text{C}$ .

Generally, the bubble adhesion force in such a low-surface-tension liquid tends to be quite low at room temperature ( $25\text{ }^{\circ}\text{C}$ ) that is why we have failed to tell the difference between a flat Cu and the MN-Cu surfaces by a classical measuring method. However, the solid-liquid-vapor contact state changes under a heating condition ( $50\text{ }^{\circ}\text{C}$ ), where forms an evaporation-induced solid-vapor interface. Although the air bubble depicts superaerophobicity at  $25\text{ }^{\circ}\text{C}$ , it could be weakened in a  $50\text{ }^{\circ}\text{C}$  heating condition, especially for the flat Cu surface with its bubble contact angle dropped from  $\sim 155^{\circ}$  to  $\sim 121^{\circ}$ . Thus, we anticipate that a strong evaporation of  $\text{C}_6\text{H}_5\text{F}_9\text{O}$  liquid contributes to enlarging the solid-vapor interface and increasing the bubble adhesion force to some extent.

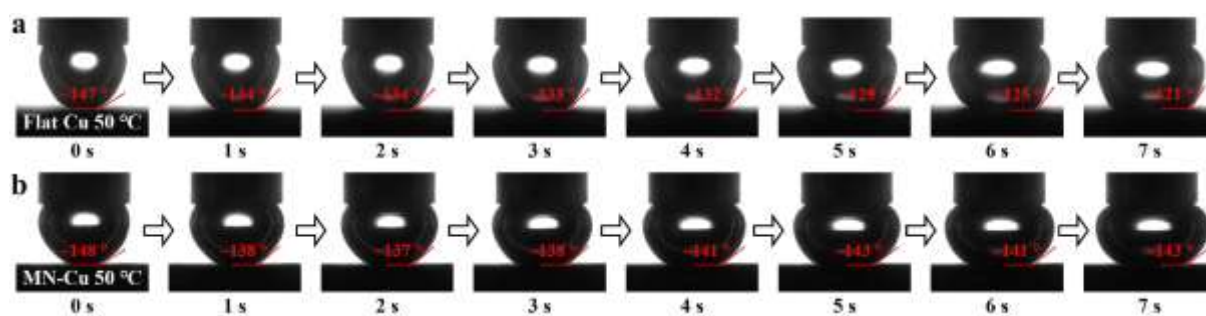


**Figure S6.** Changes of the contact state between an expanding air bubble and the 50 °C solid substrate over time, related to Movie S2 and Movie S3. (a) Flat Cu; (b) MN-Cu.

The bubble adhesion force of MN-Cu surface under  $C_6H_5F_9O$  liquid first increases, maintains at a relative stable level of 8~10  $\mu\text{N}$  until  $\sim 3$  s, and then falls down to the final 1.3  $\mu\text{N}$ . Thus, we speculate that the subsequent adhesion force drop after 3 s might be caused by formation of liquid-vapor interfaces. In contrast with the constant decrease of contact angle on a flat Cu surface, the contact angle on the MN-Cu surface exhibits an apparent rebound 3 seconds later, also indicating that multiple liquid-vapor interfaces would be formed.

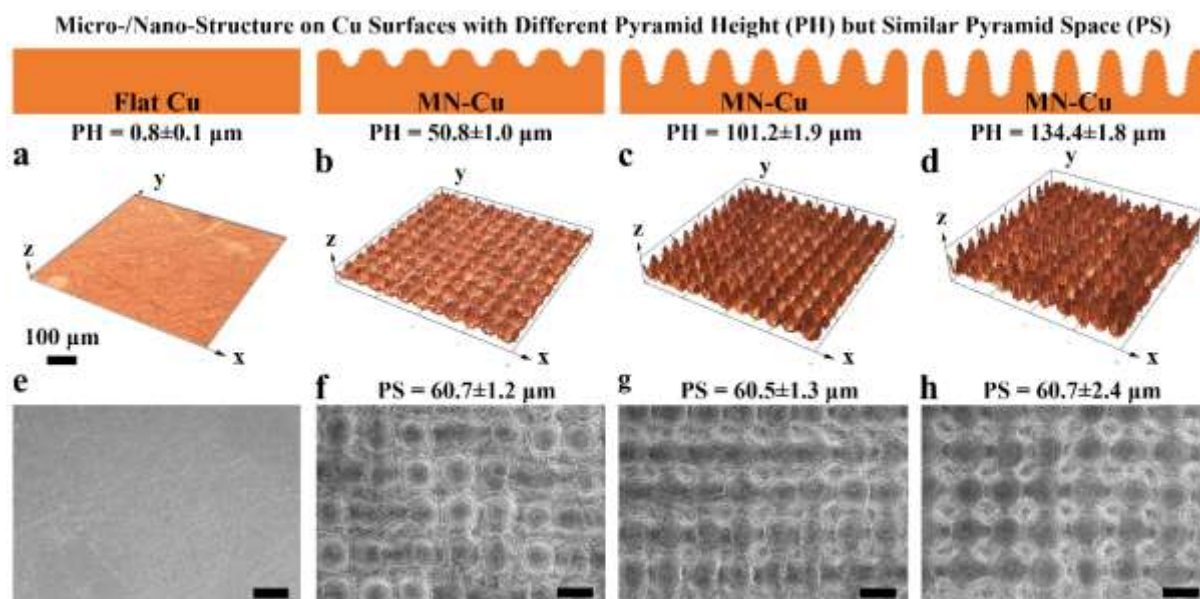


**Figure S7.** 3D Morphology and SEM images of the Cu surfaces with different pyramid height (PH) but similar pyramid space (PS), involving (a, e) flat Cu ( $PH = 0.8 \pm 0.1 \mu\text{m}$ ) surface and different MN-Cu surfaces with variable pyramid height (b, f)  $PH = 50.8 \pm 1.0 \mu\text{m}$ , (c, g)  $PH = 101.2 \pm 1.9 \mu\text{m}$ , and (d, h)  $PH = 134.4 \pm 1.8 \mu\text{m}$ , scale bar of the SEM images  $50 \mu\text{m}$ .

Compared with the increase of pyramid height, other structural parameters, such as the width and space of micro-grooves/pyramids as well as the distribution of nano-wrinkles, are kept few changes.

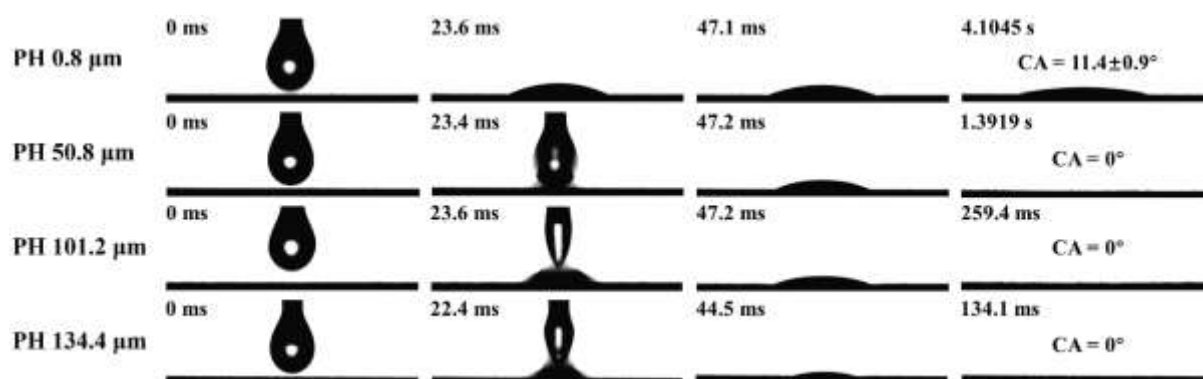


**Figure S8.** Static contact angle (CA) and spreading time of the Cu surfaces with different pyramid height (PH 0.8, 50.8, 101.2, and 134.4  $\mu\text{m}$ , respectively).

CA of a 2  $\mu\text{L}$   $\text{C}_6\text{H}_5\text{F}_9\text{O}$  droplet on flat Cu (PH 0.8  $\mu\text{m}$ ) is  $11.4 \pm 0.9^\circ$  within 4.1045 s, but CAs on MN-Cu surfaces with increasing PH (50.8, 101.2, and 134.4  $\mu\text{m}$ , respectively) are quickly up to  $\sim 0^\circ$ . The larger pyramid height possesses, the shorter spreading time (1.3919s, 259.4 ms, and 134.1 ms) takes.

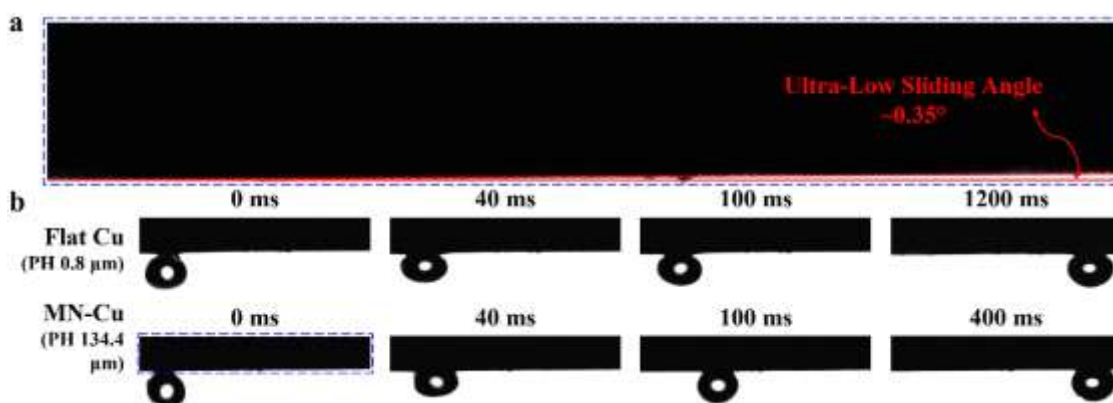


**Figure S9.** Sliding time of a 5  $\mu\text{L}$  air bubble along the slightly sloping ( $\sim 0.35^\circ$ ) flat Cu (PH  $\sim 0.8 \mu\text{m}$ ) and MN-Cu (PH  $\sim 134.4 \mu\text{m}$ ) surfaces under  $\text{C}_6\text{H}_5\text{F}_9\text{O}$  liquid. (a) Measurement of the ultra-low sloping angle of surfaces  $\sim 0.35^\circ$ ; (b) Comparison on the sliding time between Flat Cu and MN-Cu surfaces.

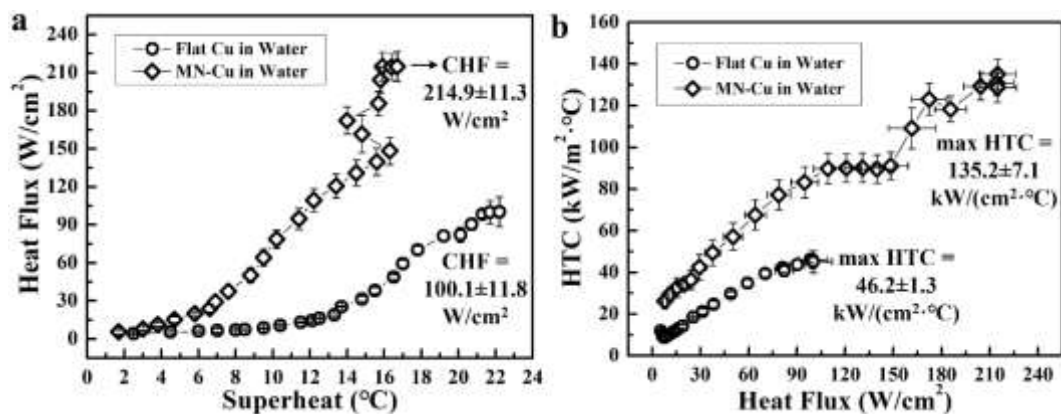


**Figure S10.** Boiling heat transfer performance of water on flat Cu (PH  $\sim 0.8 \mu\text{m}$ ) and MN-Cu (PH  $\sim 134.4 \mu\text{m}$ ) surfaces. (a) Critical heat flux (CHF); (b) Heat-transfer coefficient (HTC).

The optimized MN-Cu surface with a high PH  $\sim 134.4 \mu\text{m}$  provides a low onset nucleation boiling point at  $6.6 ^{\circ}\text{C}$ , with the CHF of  $214.9 \pm 11.3 \text{ W}/\text{cm}^2$ , and the maximum HTC of  $135.2 \pm 7.1 \text{ kW}/(\text{m}^2 \cdot ^{\circ}\text{C})$  for the pool boiling of water. Compared with a flat surface, it could be found that MN-Cu surface can promote the pool boiling by simultaneous enhancement of CHF by up to 115% and HTC by up to 193%, respectively. On the one hand, the phase-change bubbles of jet-flow boiling are confined into the micro-grooves, where the mutual coalescence is greatly suppressed and a high CHF is obtained. On the other hand, the rich nano-wrinkles around micro-pyramids provide a high nucleation site density, which promotes the evaporation for HTC enhancement.

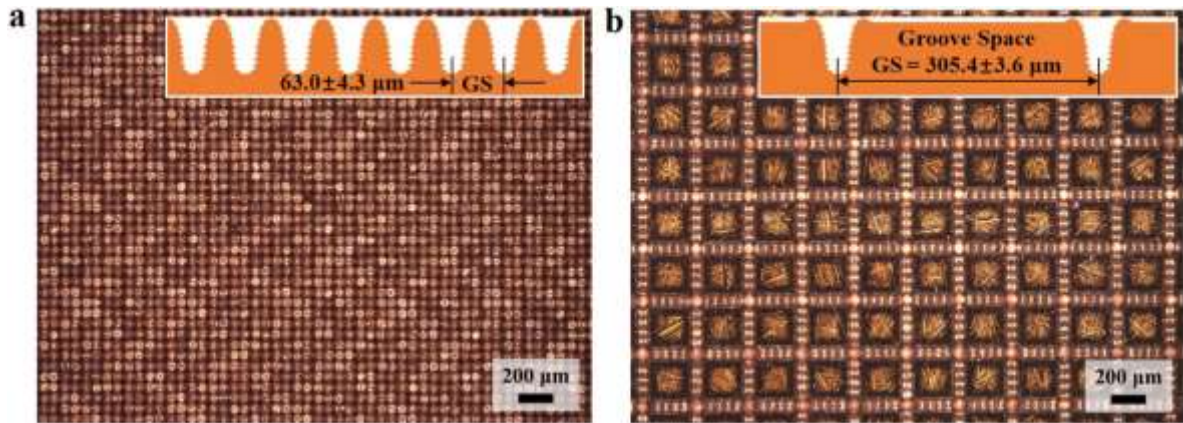


**Figure S11.** Optical microscopy images of MN-Cu surfaces with different groove space (GS) via a nano-second pulse laser fabrication. (a)  $GS = 63.0 \pm 4.3 \mu\text{m}$ ; (b)  $GS = 305.4 \pm 3.6 \mu\text{m}$ .

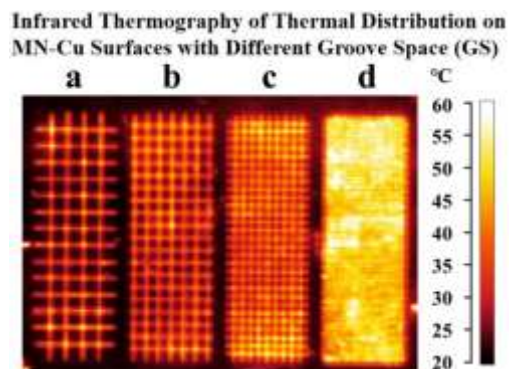


**Figure S12.** *In situ* infrared thermograph of different hot MN-Cu surfaces with controllable groove space (GS) at a structure region  $5\text{ mm} \times 15\text{ mm}$ . (a)  $GS = 1218.9 \pm 4.1\ \mu\text{m}$ ; (b)  $GS = 915.3 \pm 5.4\ \mu\text{m}$ ; (c)  $GS = 612.4 \pm 5.3\ \mu\text{m}$ ; (d)  $GS = 305.4 \pm 3.6\ \mu\text{m}$ .

It is noticeable that the bottom of micro-grooves provides larger superheat than the topside of micro-mastoids, regarding as the phase-change bubble nucleation sites of jet-flow boiling.

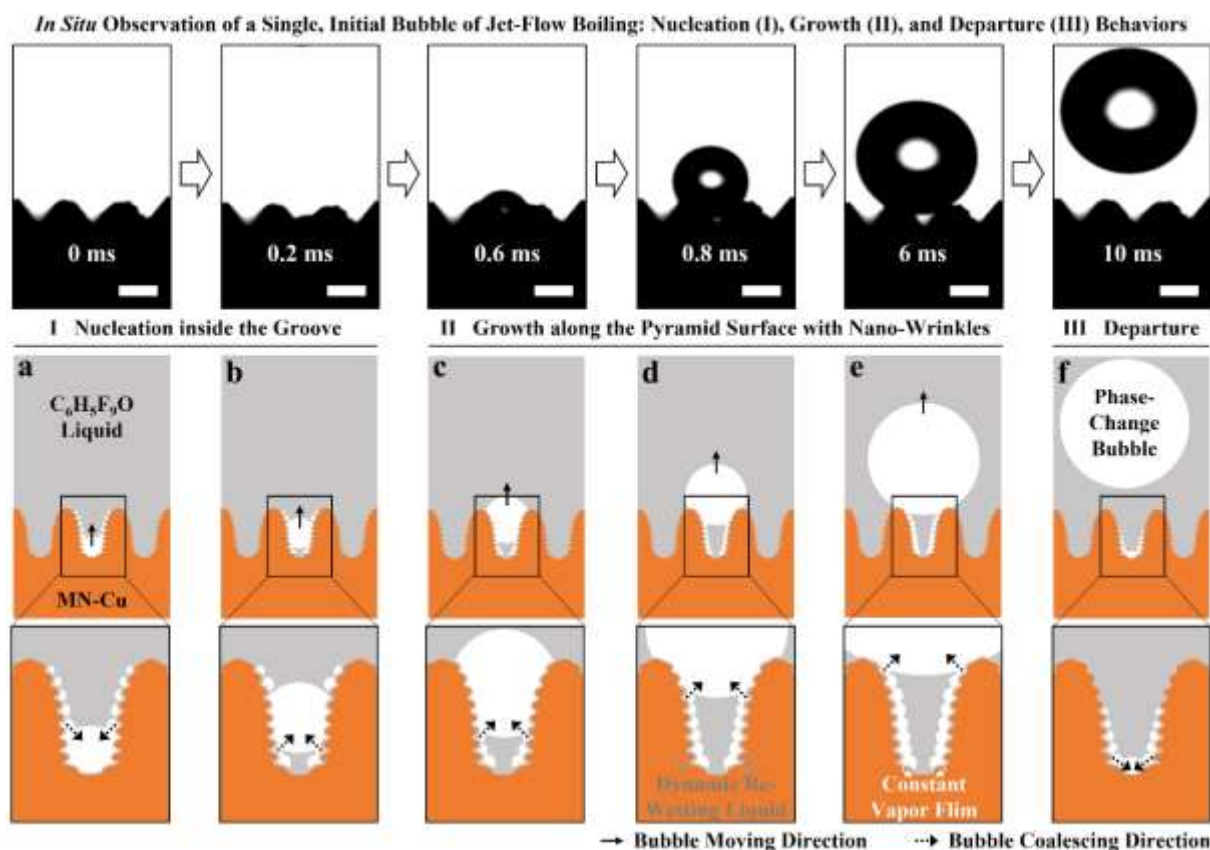


**Figure S13.** *In situ* observation and mechanism analysis of an initial jet-flow boiling bubble on a MN-Cu surface: nucleation (I) inside the micro-groove, growth (II) along the pyramid array surface with rich nano-wrinkles, and final departure (III) from the top of micro-pyramids, scale bar 50  $\mu\text{m}$ . (a) Phase-change bubble firstly forms a micro-nucleus at the bottom of micro-groove by coalescing a large number of submicro-nuclei from the surrounding nano-wrinkles because of large superheat; (b) The micro-sized bubble moves upwards owing to buoyant force in such a super-spreading system larger than under-liquid bubble adhesion force; (c) The bubble grows along the pyramid surfaces by carrying away numerous submicro-nuclei on nano-wrinkles; (d) As the micro-sized bubble moves away, dynamic re-wetting liquid simultaneously immerses into the micro-channels surrounded by pyramids and grooves by the excellent super-spreading capacity; (e) Ultra-fast dynamic re-wetting liquid layer spread along nano-wrinkles on micro-grooves/pyramids plays a key contribution for creating a constant phase-change vapor film to supply bubble growth, promote latent heat exchange, and improve heat transfer environment; (f) After the grown micro-sized bubble finally departs from the top of micro-pyramid, discrete initial vapor nuclei on the nano-wrinkles merged again at the bottom of micro-grooves.

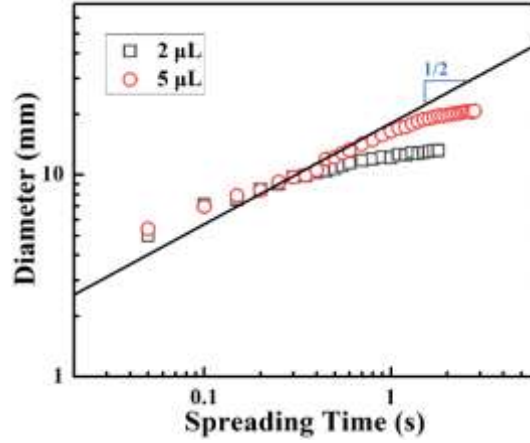


**Figure S14.** Logarithmic plot of the spreading diameter of  $C_6H_5F_9O$  liquid versus spreading time on the MN-Cu surface, the solid line indicates a power law of  $1/2$ .

The curve of liquid spreading diameter versus spreading time (SDST)<sup>[4]</sup> is characterized to investigate the dynamic spreading process based on our micro-/nanostructures. We conclude that the super-spreading rate is much larger than the evaporation rate, which results in the special jet-flow boiling phenomenon.

The evaporation rate ( $v_E$ ) can be calculated according to the following equation (9):

$$v_E = \frac{4\rho_g\pi R^3}{3\Delta t} = 8.21 \times 10^{-6} \text{ g/s} \quad (9)$$

where  $R$  and  $\Delta t$  represent the radius of gas bubble and the vaporization time in Figure 3 c, whose values are  $85 \mu\text{m}$  and  $6 \text{ ms}$ , respectively.  $\rho_g$  is the vapor density of  $C_6H_5F_9O$ , estimated as  $1.365 \text{ g/L}$ .

The superspreading rate ( $v_S$ ) is given by the equation (10) as follow:

$$v_S = \frac{\rho_l \Delta V}{\Delta t} = 2.03 \times 10^{-2} \text{ g/s} \quad (10)$$

where  $\rho_l$  is the density of  $C_6H_5F_9O$  liquid which is equal to  $1.365 \text{ g/mL}$ . As shown in Figure 2 a,  $\Delta V$  and  $\Delta t$  are the volume of liquid and the superspreading time, whose values are  $2 \mu\text{L}$  and  $134.1 \text{ ms}$ , respectively.

As discussed in our previous work,<sup>[5]</sup> we deduce the spreading distance ( $l$ ) in the array structure by comparing the change rate of free energy and the dissipation rate of viscous energy and found that it follows the classic Lucas-Washburn scaling law (11):

$$l = \sqrt{\frac{4\pi r \gamma \cos\theta_E}{f(c)\eta} t} \quad (11)$$

where  $r$ ,  $\gamma$ ,  $\theta_E$ ,  $f(c)$ , and  $\eta$  represent the radius of micro-pyramids, the surface tension of  $C_6H_5F_9O$  liquid, the intrinsic contact angle of substrate material, a numerical factor and the viscosity of the fluid, respectively.

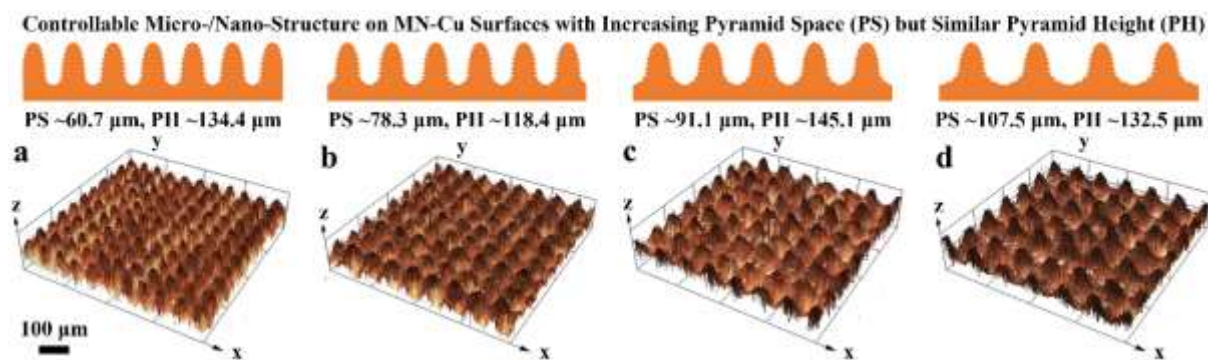


**Figure S15.** 3D Morphology images of different MN-Cu surfaces with increasing pyramid space (PS) but relatively similar pyramid height (PH) tuned by a pulse-overlapped laser-fabricating route. (a) PS ~60.7  $\mu\text{m}$ , PH ~134.4  $\mu\text{m}$ ; (b) PS ~78.3  $\mu\text{m}$ , PH ~118.4  $\mu\text{m}$ ; (c) PS ~91.1  $\mu\text{m}$ , PH ~145.1  $\mu\text{m}$ ; (d) PS ~107.5  $\mu\text{m}$ , PH ~132.5  $\mu\text{m}$ .

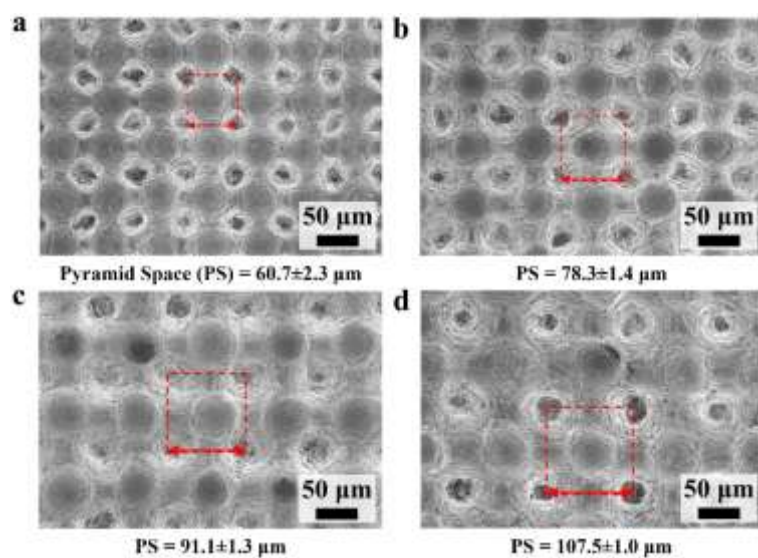


**Figure S16.** SEM image of MN-Cu surfaces with controllable pyramid space (PS) but similar pyramid height (average PH  $\sim 134.4$  μm). (a) PS =  $60.7 \pm 2.3$  μm; (b) PS =  $78.3 \pm 1.4$  μm; (c) PS =  $91.1 \pm 1.3$  μm; (d) PS =  $107.5 \pm 1.0$  μm.

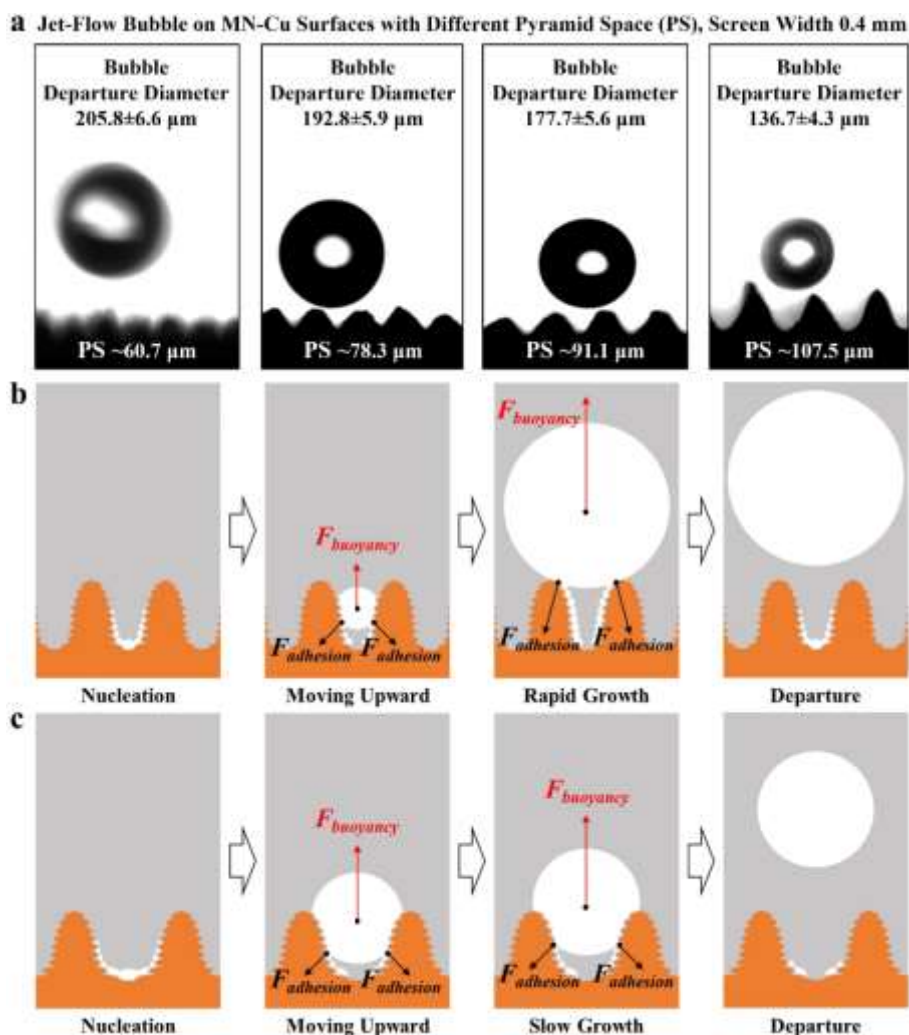


**Figure S17.** Comparison on departure diameter of an initial phase-change vapor bubble away from different MN-Cu surfaces with controllable pyramid space (PS) under  $C_6H_5F_9O$  liquid. (a) High-speed camera images; (b) Force analysis of the nucleation, growth, and departure of jet-flow boiling bubbles on a narrow PS surface; (c) Force analysis of the nucleation, growth, and departure of jet-flow boiling bubbles on a wide PS surface.

By *in situ* observation of the nucleation, growth, and departure of jet-flow bubbles, we find that phase-change bubble generally departs from the topside of micro-pyramids. However, the actual bubble departure position descends with the increase of pyramid space before growing up completely. A force analysis of phase-change bubble can easily explain this phenomenon. When the bottom of phase-change bubble moving upward at the same position with similar adhesion force value, the bubble volume on a wide PS surface is larger than that on a narrow one, meaning that the buoyancy force strongly increases and leads to the final bubble departure. On the contrary, the lower buoyancy force on a narrow PS surface makes the bubble keep moving to the top and receiving a constant vapor supply from the nano-wrinkles at the same time; thus, bubble departure diameter is larger.



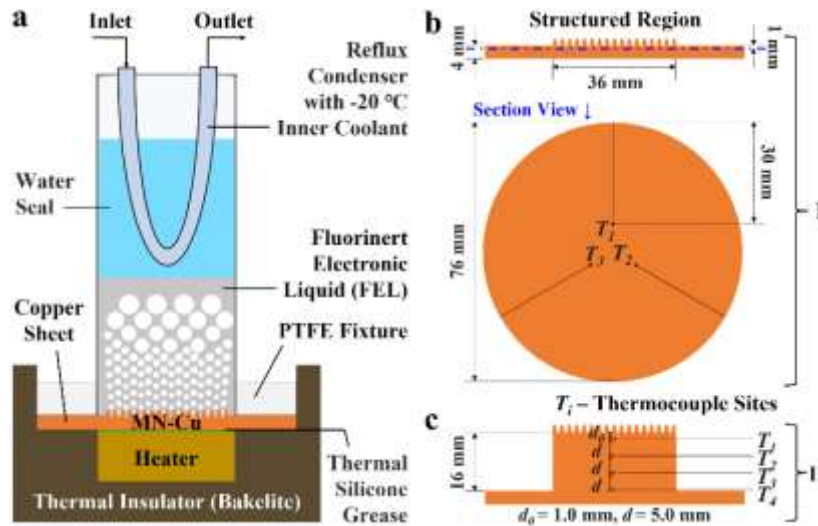


**Figure S18.** Phase-change cooling performance experimental setup. (a) Schematic diagram of the device, consisting of a heating device, a boiling chamber, and a condensation system; (b) Dimension parameters and the placement of thermocouples of a standard copper sheet (I) for the phase-change cooling performance measurement; (c) Information of a special copper sheet (II) used for observing the phase-change bubbles from a horizontal view.

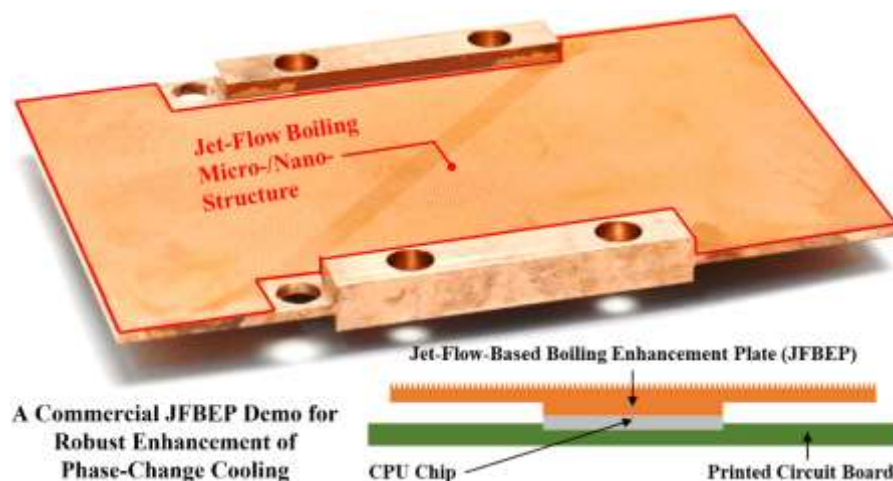


**Figure S19.** Real demo of a commercial jet-flow-based boiling enhancement plate (JFBEP) for high-performance CPU phase-change cooling, equipped by compacting with a CPU chip on a printed circuit board for efficient boiling heat transfer.

Generally, the heat flux level of  $100\sim 1000\text{ W/cm}^2$  covers the cooling heat flux requirements for most of electronics, such as high-performance supercomputers, power devices, electric vehicles, and advanced military avionics.<sup>[6,7]</sup> In our case, the average heat flux of a packaged CPU chip is no less than  $80\text{--}110\text{ W/cm}^2$  and the local heat flux inside the CPU package is estimated up to  $\sim 400\text{ W/cm}^2$  in a sudden. Thus, phase-change cooling based on a two-phase flow is adequate for this task.<sup>[8]</sup> By taking the advantages of super-spreading of commercial FELs, we have designed and produced a type of jet-flow-based boiling enhancement plate (JFBEP) demo that is several times larger than the upper surface area of a CPU chip to assist the phase-change cooling for supercomputer. Due to the durability and reliability of the laser-fabricated structures, our JFBEP products exhibits lower temperature of CPU chips and much less temperature turbulence than the previous boiling enhancement products. Furthermore, we have established a batch production with a capacity of 1000 pieces/day based on a granted and transferred Chinese invention patent (e.g.: ZL 201910217150.0), and supplied a large number of JFBEP products for the national data centers in China. Power usage effectiveness (PUE), as an international standard first developed by The Green Grid and others in 2007, is the most widely accepted way of measuring the energy efficiency of a supercomputer data center. It measures the ratio of the energy used by the information technology (IT) equipment to the energy used by the entire data center. We receive our data of  $\text{PUE} < 1.04$  from an authorized organization (National Supercomputing Center in Xi'an, China) by monitoring the power consumption equipped our jet-flow-based boiling enhanced products exclusively in a phase-change cooling system. It is much lower than that by either a single-phase liquid cooling ( $\sim 1.17$ , from Beijing Energy Conservation and Environmental Protection Center, China) or a

conventional air cooling (>1.55, from 2007 to 2022 according to the report from the Uptime Institute).<sup>[9]</sup> In addition, the world's average datacenter's PUE rating in 2020 was 1.58 and the figure has been stagnant since 2013.<sup>[10]</sup>

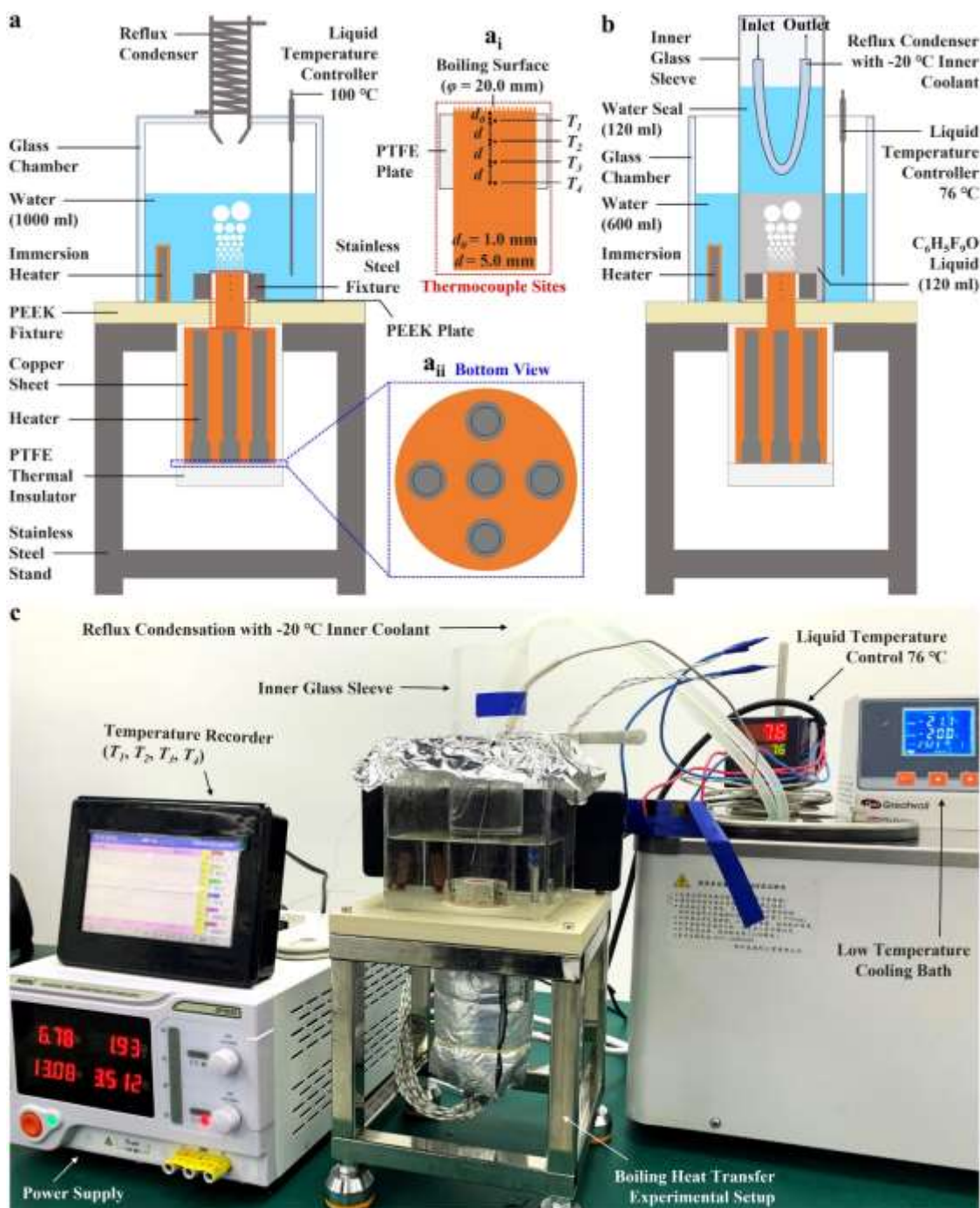


**Figure S20.** Boiling heat transfer performance experimental setup. (a) A basic pool boiling device for water with magnified schematics elucidating the ( $a_i$ ) detailed information of thermocouple sites and the ( $a_{ii}$ ) placement of heating rods inside the copper sheet; (b) A modified pool boiling device for  $C_6H_5F_9O$  by adding an inner glass sleeve to save the dosage of liquid and applying a water condensation seal to prevent the escape of evaporated liquid; (c) An actual photograph of pool boiling apparatus for  $C_6H_5F_9O$  after 60 min pre-heating at 76 °C.

**Table S1.** Comparison on enhanced boiling heat transfer performance of the previously reported micro-/nanostructured Cu surfaces.

Authors	Working Fluid	CHF [W/cm <sup>2</sup> ]	$\Delta$ CHF [%]	HTC [kW/(cm <sup>2</sup> ·°C)]	$\Delta$ HTC [%]
Li et al. <sup>[11]</sup>	Water	160.0	+67	133.0	+59
Chen et al. <sup>[12]</sup>	Water	200.0	N/A	61.5	N/A
Xu et al. <sup>[13]</sup>	Water	239.0	+101	59.0	+120
Wen et al. <sup>[14]</sup>	Water	250.0	+71	87.0	+172
Kruse et al. <sup>[15]</sup>	Water	143.0	-15	87.0	+24
Može et al. <sup>[16]</sup>	Water	158.0	+89	76.1	+129
Mani et al. <sup>[17]</sup>	Water	226.0	+103	97.5	+153
Ze et al. <sup>[18]</sup>	Water	272.0	+64	109.4	+142
This Work	Water	214.9	+115	135.2	+193
Byon et al. <sup>[19]</sup>	FEL: FC-72	45.1	+72	N/A	N/A
El-Genk et al. <sup>[20]</sup>	FEL: PF-5060	26.4	+59	N/A	N/A
El-Genk et al. <sup>[21]</sup>	FEL: PF-5060	19.3	+22.9	10.6	+58.2
El-Genk et al. <sup>[22]</sup>	FEL: HFE-7000	30.9	+49	22.0	+250
Može et al. <sup>[23]</sup>	FEL: Novec 649	25.0	+14	13.0	+54
Kaniowski et al. <sup>[24]</sup>	FEL: FC-72	27.2	N/A	25.0	N/A
Fan et al. <sup>[25]</sup>	FEL: Novec 7100	52.2	+40	N/A	-20
Jiang et al. <sup>[26]</sup>	FEL: HFE-7100	49.0	+82	22.0	+144
This Work	FEL: C <sub>6</sub> H <sub>5</sub> F <sub>9</sub> O	42.6	+80	72.9	+608

CHF - Critical Heat Flux; HTC - Heat Transfer Coefficient; FEL - Fluorinert Electronic Liquid;  
 $\Delta$ CHF,  $\Delta$ HTC - increase of CHF, HTC compared with smooth surface.

Herein, we summarize the enhanced boiling CHF and HTC of either water or FELs based on micro-/nanostructured copper structures according to previously reported literatures, and find that our optimized MN-Cu surface possesses the highest  $\Delta$ CHF and also the highest  $\Delta$ HTC, which might be a more equitable evaluation index to avoid the deviation of absolute value from different experimental conditions and measuring methods.<sup>[27]</sup>

**Table S2.** Basic properties of three different commercial fluorinert electronic liquids (FELs) from 3M company, USA.

Parameter	Unit	3M <sup>™</sup> Novec <sup>™</sup> Engineered Fluids		
		7100	7200	7300
Boiling Point	°C	61	76	98
Molecular Weight	g/mol	250	264	350
Vapor Pressure	kPa	27	16	5.9
Heat of Vaporization	kJ/kg	112	119	102
Liquid Density	kg/m <sup>3</sup>	1510	1420	1660
Absolute Viscosity	cP	0.58	0.58	1.18
Specific Heat	J/kg-K	1183	1220	1140
Surface Tension	mN/m	13.6	13.6	15.0
Solubility of Water in Fluid	ppm by weight	95	92	67
Dielectric Constant @ 1 kHz	-	7.4	7.3	6.1
Volume Resistivity	Ohm-cm	10 <sup>8</sup>	10 <sup>8</sup>	10 <sup>11</sup>

<https://www.3M.com/electronics>, 3M 2020

**Movie S1.** Super-spreading of a 2  $\mu\text{L}$   $\text{C}_6\text{H}_5\text{F}_9\text{O}$  liquid droplet on MN-Cu surface, 1/2 slow play.

**Movie S2.** Dynamic under-liquid bubble adhesion process of an expanding bubble ( $\sim 2.1 \mu\text{L} \sim 3.6 \mu\text{L}$ ) on flat Cu surface at 50 °C in  $\text{C}_6\text{H}_5\text{F}_9\text{O}$  liquid.

**Movie S3.** Dynamic under-liquid bubble adhesion process of an expanding bubble ( $\sim 2.1 \mu\text{L} \sim 3.6 \mu\text{L}$ ) on MN-Cu surface at 50 °C in  $\text{C}_6\text{H}_5\text{F}_9\text{O}$  liquid.

**Movie S4.** *In situ* boiling comparison of a Cu plate with asymmetric structures in  $\text{C}_6\text{H}_5\text{F}_9\text{O}$  liquid at a low superheat  $\sim 3.0$  °C (left panel: flat Cu; right panel: MN-Cu with the PH  $\sim 134.4 \mu\text{m}$ ).

**Movie S5.** Rolling and coalescence of the onset of jet-flow boiling (OJB) bubbles on a flat Cu surface, leading to a wider bubble diameter distribution without structural confinement effect.

**Movie S6.** A single strip of jet-flow boiling bubbles ejected from the bottom of micro-groove on a designed MN-Cu surface (PS  $\sim 60.7 \mu\text{m}$ ; PH  $\sim 134.4 \mu\text{m}$ ), 1/25 slow play.

**Movie S7.** *In situ* observation of nucleation, growth, and departure behaviors of an initial jet-flow boiling bubble on a designed MN-Cu surface with narrow pyramid space (PS  $\sim 78.3 \mu\text{m}$ ), 1/250 slow play.

**Movie S8.** *In situ* observation of nucleation, growth, and departure behaviors of an initial jet-flow boiling bubble on a designed MN-Cu surface with wide pyramid space (PS  $\sim 107.5 \mu\text{m}$ ), 1/250 slow play.

## References

- [1] H. J. Butt, I. V. Roisman, M. Brinkmann, P. Papadopoulos, D. Vollmer, C. Semperebon, *Curr. Opin. Colloid In.* **2014**, *19*, 343.
- [2] H. J. Butt, M. Kappl, *Adv. Colloid Interfac.* **2009**, *146*, 48.
- [3] B. Song, J. Springer, *J. Colloid Interface Sci.* **1996**, *184*, 64.
- [4] W. Miao, Y. Tian, L. Jiang, *Acc. Chem. Res.* **2022**, *55*, 1467.
- [5] W. Miao, S. Zheng, J. Zhou, B. Zhang, R. Fan, D. Hao, L. Sun, D. Wang, Z. Zhu, X. Jin, Y. Tian, L. Jiang, *Adv. Mater.* **2021**, *33*, 2007152.
- [6] I. Mudawar, *IEEE T. Compon. Pack. T.* **2001**, *24*, 122.
- [7] S. Fan, F. Duan, *Int. J. Heat Mass Transfer* **2020**, *150*, 119324.
- [8] S. Greengard, *Commun. ACM* **2022**, *65*, 24.
- [9] J. Davis, D. Bizo, A. Lawrence, O. Rogers, M. Smolaks, L. Simon, D. Donnellan, Uptime Institute Global Data Center Survey Results 2022, <https://uptimeinstitute.com/resources/research-and-reports/uptime-institute-global-data-center-survey-results-2022>, September 14, **2022**.
- [10] A. Lawrence, Data center PUEs flat since 2013, <https://journal.uptimeinstitute.com/data-center-pues-flat-since-2013/>, April 27, **2020**.
- [11] C. Li, Z. K. Wang, P. I. Wang, Y. Peles, N. Koratkar, G. P. Peterson, *Small* **2008**, *8*, 1084.
- [12] R. K. Chen, M. C. Lu, V. Srinivasan, Z. J. Wang, H. H. Cho, A. Majumdar, *Nano Lett.* **2009**, *9*, 548.
- [13] P. F. Xu, Q. Li, Y. M. Xuan, *Int. J. Heat Mass Transfer* **2015**, *80*, 107.
- [14] R. Wen, Q. Li, W. Wang, B. Latour, C. H. Li, C. Li, Y.-C. Lee, R. Yang, *Nano Energy* **2017**, *38*, 59.
- [15] C. Kruse, A. Tsubaki, C. Zuhlke, D. Alexander, M. Anderson, E. Peng, J. Shield, S. Ndao, G. Gogos, *J. Heat Transfer* **2019**, *141*, 051503.
- [16] M. Može, M. Zupančič, M. Hočevar, I. Golobič, P. Gregorčič, *Appl. Surf. Sci.* **2019**, *490*, 220.
- [17] D. Mani, S. Sivan, H. M. Ali, U. K. Ganesan, *Int. J. Photoenergy* **2020**, *2020*, 3846157.
- [18] H. Ze, F. Wu, S. Chen, X. Gao, *Adv. Mater. Interfaces* **2020**, *7*, 2000482.
- [19] C. Byon, S. Choi, S. J. Kim, *Int. J. Heat Mass Transfer* **2013**, *65*, 655.
- [20] M. S. El-Genk, A. F. Ali, *J. Heat Transfer* **2015**, *137*, 041501.
- [21] M. S. El-Genk, A. Suszko, *Int. J. Heat Mass Transfer* **2016**, *95*, 650.
- [22] M. S. El-Genk, M. Pourghasemi, *Int. J. Heat Mass Transfer* **2021**, *164*, 120540.

- [23] M. Može, V. Vajc, M. Zupančič, I. Golobič, *Nanomaterials* **2021**, *11*, 3216.
- [24] R. Kaniowski, R. Pastuszko, *Energies* **2021**, *14*, 7283.
- [25] S. Fan, W. Tong, F. Duan, *Int. Commun. Heat Mass* **2021**, *122*, 105166.
- [26] Y. Jiang, G. Zhou, J. Zhou, F. Zhou, X. Huai, *Appl. Therm. Eng.* **2022**, *216*, 119067.
- [27] M. Može, M. Senegačnik, P. Gregorčič, M. Hočevar, M. Zupančič, I. Golobič, *ACS Appl. Mater. Interfaces* **2020**, *12*, 24419.